J Mater Sci: Mater Electron (2017) 28:8255–8265
DOI 10.1007/s10854-017-6538-x

Ball-milling combined calcination synthesis of In_2O_3/C_3N_4 for high photocatalytic activity under visible light irradiation

Rongxian Zhang[1] · Xiaogang Lu[1] · Liying Huang[1] · Zhijiang Ke[1] · Yeping Li[2]

Received: 11 December 2016 / Accepted: 2 February 2017 / Published online: 25 February 2017

Abstract In_2O_3/C_3N_4 composites were prepared with $In(OH)_3$ and C_3N_4 by ball-milling calcination. The samples were characterized by TG, XRD, TEM, XPS, FT-IR, DRS, EIS, Photocurrent and Photoluminescence measurements. Photocatalytic performance of the catalyst was measured by the degradation test of methyl orange (MO). The photocatalytic performance of In_2O_3/C_3N_4 composites is higher than that of In_2O_3 and C_3N_4. The photocurrent response to In_2O_3/C_3 N_4 (17.3%) was 11.3 times and 183.1 times as high as that of pure In_2O_3 and C_3N_4, respectively. The enhanced photocatalytic activity was attributed to the high separation and migration efficiency of photoinduced electrons and holes. Superoxide anion ($\cdot O_2^-$) and hole (h^+) played important roles in the methyl orange (MO) degradation.

1 Introduction

The environmental issues and energy shortages have become two important global problems, which have seriously threatened people's life. Photocatalytic technology is an attractive process to solve the problems. TiO_2 is one of the most attractive semiconductors, which has already been used in catalysis, sensing, hydrogen production and optical electronics. However, TiO_2 could only use UV light to stimulate its catalytic performance [1]. Therefore, it has an important practical value to prepare photocatalytic materials with high activity under visible light.

Indium oxide (In_2O_3), a n-type semiconductor material, has a direct band gap of 3.8 eV and an indirect band gap of 2.8 eV [2]. It is an effective sensitizer and its absorption spectrum can extend from ultraviolet region to the visible region. It has been widely used in solar cells [3], flat panel display [4], gas sensor [5]. However, due to the high electron–hole recombination rate, the efficiency of In_2O_3 is still limited. In order to improve the photocatalytic activity of In_2O_3, researchers have used a variety of methods, such as morphology control [6, 7], metal deposition [8], and combining with semiconductors [9–11].

Graphitic carbon nitride (denoted as C_3N_4) is a kind of medium band gap (2.7 eV) nonmetal photocatalyst [12]. It has good chemical stability and thermal stability. Furthermore, it can be used to split water into H_2 and O_2 and degrade organic pollutants under visible light irradiation [13]. But high photoproduction electron–hole recombination rate seriously affects the catalytic properties of C_3N_4. C_3N_4 can be easily adhered on the surface of other compounds due to its softness. Deferent types of strategies have been used to make the catalytic properties of C_3N_4 better, including coupling with metals [14–16] and semiconductor materials such as AgX (X = Cl, Br, I) [17–19], ZnO [20], CdS [21], WO_3 [22], Co_3O_4 [23], Ag_3PO_4 [24], BiOX [25–28] and SnO_2 [29]. Compared with the original semiconductor materials, the photocatalytic performance of these composites were enhanced obviously. Through mechanism analyzing, the reason for photocatalytic performance enhancements may be the improvement of electron–hole migration and separation.

Recently, some investigations about In_2O_3/C_3N_4 were reported. In_2O_3/C_3N_4 composites can be used for hydrogen evolution [30], CO_2 reduction [30] and Rhodamine B (Rhb)

✉ Rongxian Zhang
rong@ujs.edu.cn

[1] School of Chemistry and Chemical Engineering, Jiangsu University, Zhenjiang 212013, People's Republic of China

[2] School of Pharmacy, Jiangsu University, Zhenjiang 212013, People's Republic of China

degradation [11]. The obtained composites showed better performance than individual In_2O_3 and C_3N_4. These catalysts were mostly prepared by complicated method in liquid phase [9] and the solid phase synthesis was rarely reported. In this work, a solid phase synthesis of In_2O_3/C_3N_4 hybrid photocatalysts by ball-milling calcination was presented. In_2O_3/C_3N_4 composites with different mass fractions of In_2O_3 were successfully prepared and characterized by various techniques. The organic pollution (MO) was chosen to examine the photocatalytic activity of In_2O_3, C_3N_4 and In_2O_3/C_3N_4 composites, which was rarely reported before. The photocatlytic reaction mechanism was also studied.

2 Experimental

2.1 Synthesis of photocatalysts

Reagents were of analytical reagent (AR) grade, which were purchased from sinopharm company sources. Distilled water was used in the whole experiment. Melamine was used as precursor to synthesize C_3N_4 powders in a muffle furnace. Typically, 5 g melamine was put in an alumina crucible with a cover, and first heated to 500 °C at a rate of 3.3 °C /min and held for 2h, subsequently the sample was kept at 550 °C for another 2 h. The bulk C_3N_4 was grounded into powder. The obtained sample was labeled as C_3N_4.

In_2O_3 powder was synthesized by heating $In(OH)_3$ in a muffle furnace. Typically, 3 g $In(OH)_3$ was put in an alumina crucible with a cover, and then heated to 500 °C (kept for 2h).

Synthesis of In_2O_3/C_3N_4 composites was as follows: C_3N_4 (1.000 g) and different amount of $In(OH)_3$ were added into a mortar and grounded for 5h with 5 ml alcohol. Then the mixed powder was dried at 65 °C for 5 h. Subsequently the mixed powder was placed in an alumina crucible with a cover, which was heated to 440 °C (kept for 2 h) and then kept at 390 °C for another 12 h. In_2O_3/C_3N_4 photocatalysts with 0.100 g, 0.200 g and 0.300 g $In(OH)_3$ were synthesized and according to the results of TG, they were named as In_2O_3/C_3N_4 (9.6%), In_2O_3/C_3N_4 (17.3%) and In_2O_3/C_3N_4 (41.2%), respectively.

2.2 Characterization

The thermogravimetric analysis (TG, STA 449 C, Germany) was performed using a thermal analyzer at a rate of 10 °C /min from 25 °C to 800 °C in the air. X-ray powder diffraction (XRD, XRD-6100, Japan) was performed in a parallel mode (7°/min, 2θ range from 10° to 80°) using a Shimadzu XRD-6000 X-ray diffractometer (Cu K source). Field emission scanning electron microscopy (SEM, JSM-6010 PLUS/LA, Japan) was used to examine the surface condition of the samples. Transmission electron microscopy (TEM, JSM-2010F, Japan) was carried out with an acceleration voltage of 200 kV to investigate the fine morphology. The element chemical valence on the surface of In_2O_3, C_3N_4 and In_2O_3/C_3 N_4 (17.3%) were investigated by X-ray photoelectron spectroscopy (XPS) for chemical analysis on a photo-electron spectrometer (ESCA Lab MKII X-ray) using the Mg Kα radiation. Fourier transform infrared spectra (FT-IR, Nicolet Nexus 470, America) was recorded on a Fourier transform infrared spectrometer at room temperature. UV–Vis diffuse reflectance spectra (DRS, UV-3600Plus, Japan) were detected on an UV–Vis spectropho-tometer and $BaSO_4$ was used as background. The degradation of MO in aqueous solutions was tracked using an UV–Vis spectroscopy (Cary 8454, America).

2.3 Photocurrent and electrochemical impedance spectroscopy (EIS) measurements

Photocurrent tests were analyzed with an electro-chemical analyzer (CHI760 D, CHI Shanghai, Inc.). The detection was operated in a conventional three-electrode unit with counter electrode, working electrode and reference. A Pt wire and Hg/Hg_2Cl_2 (in saturated KCl) were used as the counter electrode and reference electrode, respectively. The working electrodes were the as-prepared samples (0.1 mg) having an active area of 0.5 cm^2. 0.1 M Na_2SO_4 was used as the electrolyte and irradiation proceeded with a LED lamp (30 W).

EIS measurements were performed in a 0.1 M KCl solution containing 5 mM $Fe(CN)_6^{3-}/(Fe(CN)_6^{4-}$ with a frequency range from 0.01 to 100 kHz at 0.24 V, and the amplitude of the applied sine wave potential in each case was 5 mV. The modified electrode was prepared in a simple method as follows: 5 mg g-C_3N_4 was dispersed 1 mL distilled water to make a g-C_3N_4 homogeneous suspension. Then, 20 μL of the slurry was dripped on the ITO glass with a 1 cm × 0.5 cm area and dried at 60 °C for 8 h (denoted as g-C_3N_4/ITO). In_2O_3/C_3N_4/ITO with the same quantities was prepared with the same procedure.

2.4 Measurement of photocatalytic properties

The photodegradation of MO was conducted in Pyrex glass vessel with a 300 W xenon lamp as light source (≥400 nm). Typically, 0.10 g of the as-prepared catalyst was dispersed in 100 ml MO solution (15mg L^{-1}) under ultrasonication for 10 min. Then, the mixture was stirred in a dark environment for 0.5 h to get an adsorption–desorption equilibrium. Moreover, 4 ml solution was taken per 30 min and then centrifuged to remove the photocatalyst particles. The

absorbance of MO in aqueous solutions was tracked by UV–Vis spectroscopy at 464 nm.

3 Results and discussion

3.1 TG analysis

The contents of In_2O_3 in In_2O_3/C_3N_4 composite material can be obtained by TG analysis and the curves were shown in Fig. 1. The mass of the pure In_2O_3 had no change within the range from 25 °C to 800 °C and In_2O_3 had good thermal stability. The weight of pure C_3N_4 decreased rapidly from 550 °C to 740 °C, indicating the thermal decomposition of C_3N_4 to generate small molecule volatile substances. The weight of In_2O_3/C_3N_4 composites decreased rapidly between 500 °C and 720 °C, corresponding to the system of C_3N_4 thermal decomposition. For In_2O_3/C_3N_4 composites, decomposition temperature of C_3N_4 was lower than that of pure C_3N_4. The result shows that it was easier to make C_3N_4 thermal decomposition due to the existence of In_2O_3, which was a oxidation catalyst that can absorb and support reactive oxygen in the air [31], and then oxidize the g-C_3N_4 at a relatively low temperature.

3.2 XRD analysis

XRD was applied to study the phase structures of C_3N_4, In_2O_3, and In_2O_3/C_3N_4 composites (Fig. 2). For C_3N_4, there were two apparent diffraction peaks at 27.3° and 13.1°, which were correspond to the typical peak of aromatic systems as the (002) peak for graphitic materials due to interlayer stacking, and the interplanar separation as the (100) peak, respectively [32]. For In_2O_3, six distinct diffraction peaks at 21.5°, 30.6°, 35.6°, 45.4°, 50.9°, and 60.8° can be observed, which were assigned to the (211), (222), (400), (431), (440), and (622) crystal planes (JCPDS No.71-2194), respectively [30]. In XRD patterns, In_2O_3/C_3N_4 composites exhibited the typical peaks of In_2O_3 and C_3N_4.

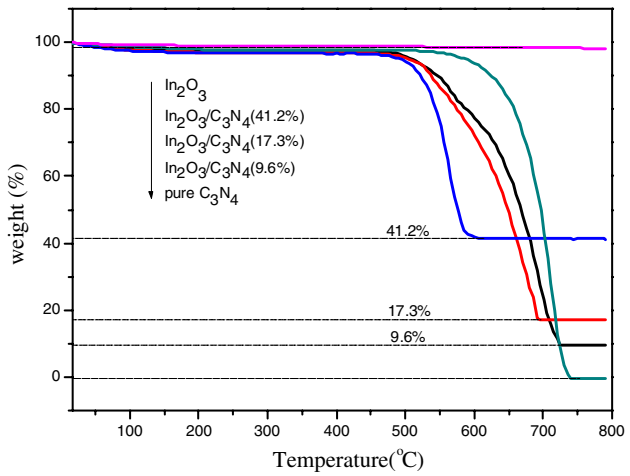

Fig. 1 TG thermograms for heating the In_2O_3/C_3N_4 composites

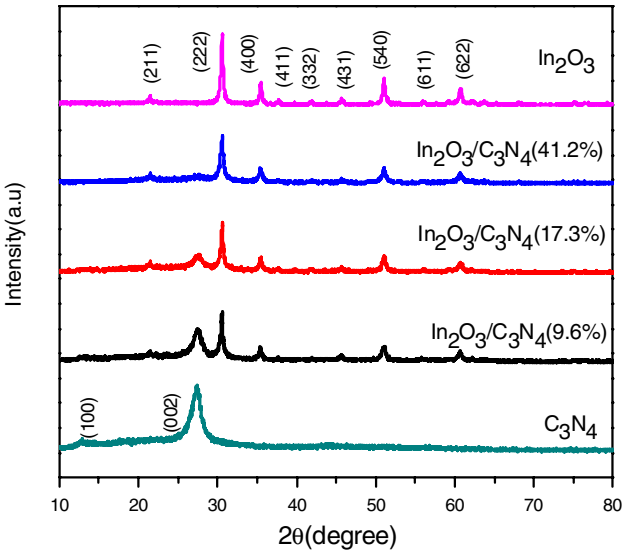

Fig. 2 XRD pattern of In_2O_3, C_3N_4 and In_2O_3/C_3N_4 composites

3.3 TEM and EDS analyses

The morphology and structure of In_2O_3, C_3N_4 and In_2O_3/C_3N_4 (17.3%) composite were analyzed by TEM (Fig. 3). The size of In_2O_3 nanoparticles ranged from 50 nm to 200 nm (Fig. 3A) and C_3N_4 displayed lamellar structure (Fig. 3B). For In_2O_3/C_3N_4 (17.3%) composite (Fig. 3C), the grey area can be assigned to C_3N_4 and black particles can be assigned to In_2O_3 nanoparticles. In order to further study the construction of In_2O_3/C_3N_4 (17.3%) composites, the enlarged TEM image (Fig. 3D) was obtained from the black box of Fig. 3C. It can be observed that In_2O_3 nanoparticles tightly attached on the surface and at edge of C_3N_4. Although the samples had been sonicated for 3 h before TEM, In_2O_3 nanoparticles were not peeled from the surface of C_3N_4, suggesting that there was a strong interaction between the In_2O_3 and C_3N_4. According to TEM analysis results, the heterojunction structure formed between In_2O_3 and C_3N_4, which played an important role in the charge transfer of the compound semiconductor materials. The morphologies of the In_2O_3/C_3N_4 (17.3%) composite were observed by SEM (Fig. 3E), in which In_2O_3/C_3N_4 (17.3%) composite showed sheet-shaped structure. The chemical composition of In_2O_3/C_3N_4 (17.3%) composite was further conformed by EDS analysis. As shown in Fig. 3F, In, O, C and N elements can be detected in this spectrum.

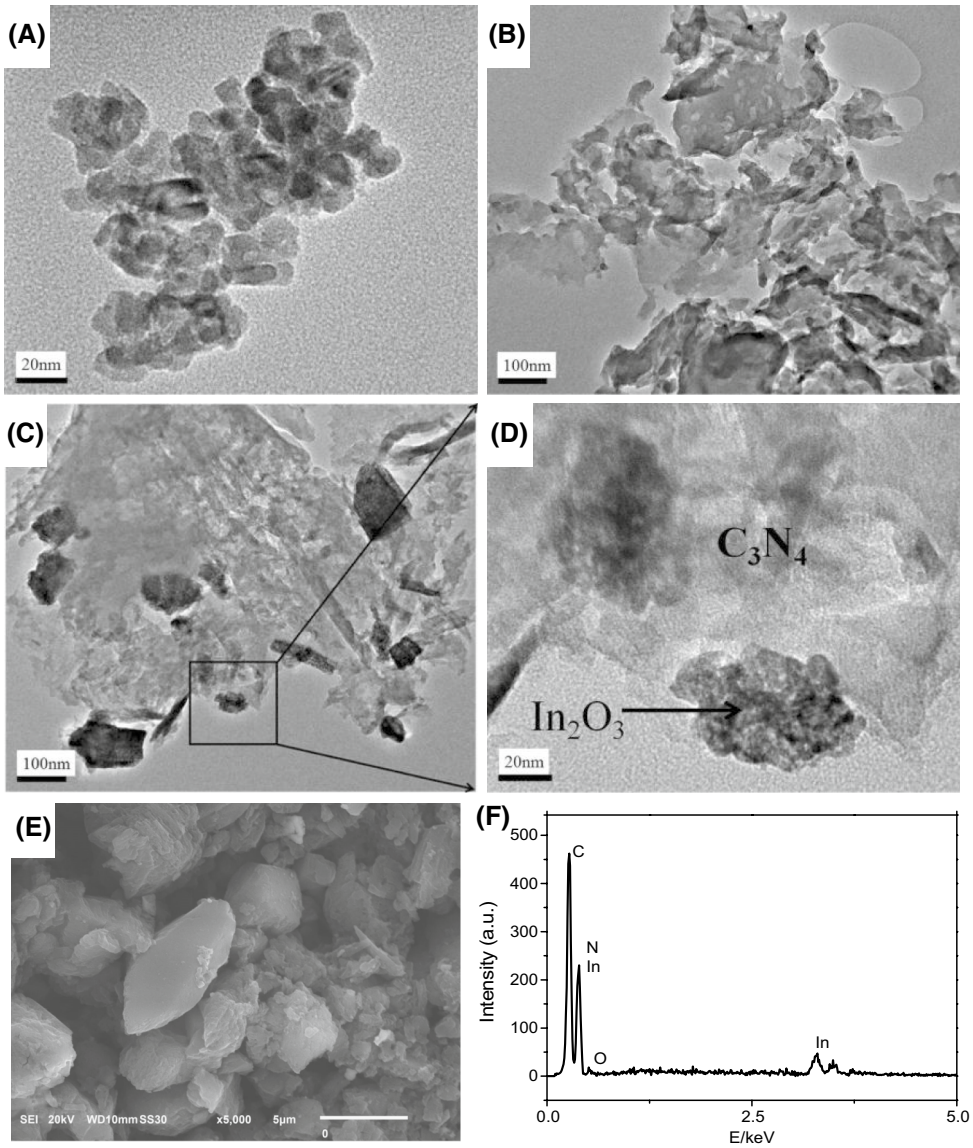

Fig. 3 TEM images of **A** In_2O_3, **B** C_3N_4, **C** In_2O_3/C_3N_4 (17.3%) composite and **D** the enlarged TEM image of **C; E** SEM and **F** EDS of In_2O_3/C_3N_4 (17.3%) composite

3.4 XPS analysis

The element chemical valence on the surface of In_2O_3, C_3N_4 and In_2O_3/C_3N_4 (17.3%) composite can be obtained by XPS. In the full spectrum, it can be observed that In_2O_3/C_3 N_4 (17.3%) composite contained In, O, C and N (Fig. 4A). High-resolution XPS analyses of In3d, O1s, C1s and N1s were used to determine the valence state of each element in In_2O_3, C_3N_4 and In_2O_3/C_3N_4 (17.3%) composite (Fig. 4B, C, D, E). The peak of In3d binding energies at 444.4 eV and 452.0 eV (Fig. 4B) can be ascribed to the In $3d_{3/2}$ and In $3d_{5/2}$, which was consistent with the spectra of In_2O_3 reported on literatures [33], and it was the characteristic binding energies of In^{3+}. Whereas, the peaks of the In $3d_{3/2}$ and In $3d_{5/2}$ in the In_2O_3/C_3 N_4 (17.3%) composite were at 444.9 eV and 452.5 eV, which both moved to a higher energy direction. The interaction between In_2O_3 and C_3N_4 may result in such a shift. In Fig. 4C, for In_2O_3, O1s peak centered at 530.0 eV and 532.3 eV, which was ascribed to the lattice oxygen and the surface hydroxyl oxygen of In_2O_3, respectively [34]. For In_2O_3/C_3 N_4 (17.3%) composite, the O1s peak was much weaker than that of In_2O_3. It may be attributed to the existence of C_3N_4. For C_3N_4, the peak of C1s at 288.2 eV was contributed to a C–N coordination (Fig. 4D). Another peak at 284.7 eV was corresponding to surface carbon [9]. The C1s peak of In_2O_3/C_3 N_4 (17.3%) composite showed a slight shift compared with pure C_3N_4, which was attributed to the interaction between In_2O_3 and C_3N_4. For both C_3N_4 and In_2O_3/C_3 N_4 (17.3%) composite, N1s (peaked) peak at 398.8 eV corresponded to sp^2 -hybridized nitrogen (C=N-C) (Fig. 4E), indicating the existence of carbon nitride [30].

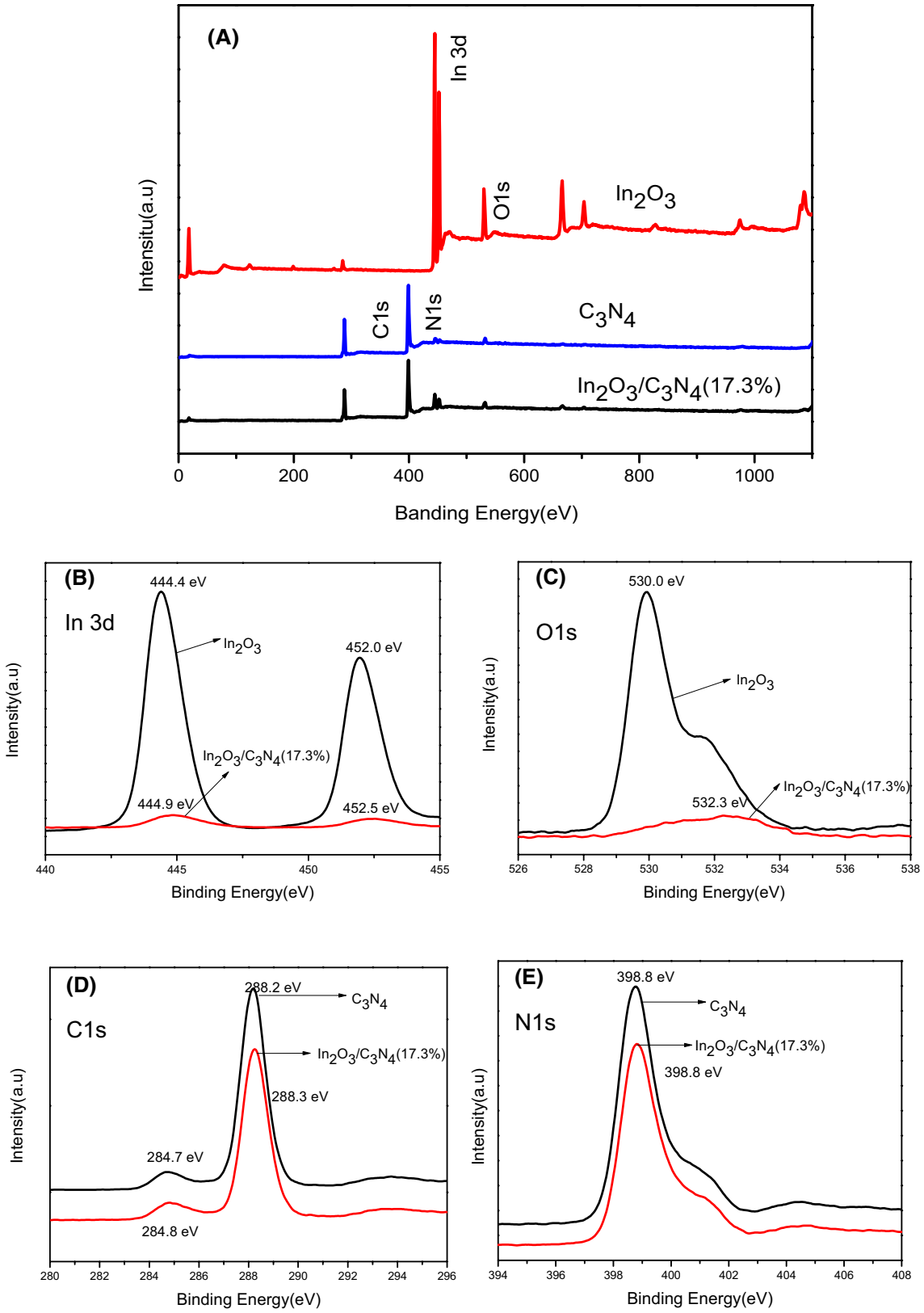

Fig. 4 XPS survey spectra of In_2O_3 and In_2O_3/C_3N_4 (17.3%) **A**; high resolution XPS spectra of In_2O_3 and In_2O_3/C_3N_4 (17.3%): **B** In3d, **C** O1s, **D** C1s and **E** N1s

3.5 FT-IR analysis

FT-IR spectra of In_2O_3, C_3N_4 and In_2O_3/C_3N_4 composites were recorded in Fig. 5. For C_3N_4,

the absorption peaks of 1240 cm^{-1}, 1321 cm^{-1}, 1558 cm^{-1}, and 1635 cm^{-1} were assigned to the characteristic stretching modes of the C-N heterocycle [35] and the typical peak at 806 cm^{-1} was assigned to triazine units [36]. For In_2O_3, a characteristic absorption peak at 562 cm^{-1} was observed, which was assigned to the presence of In-O phonon vibration [37]. For In_2O_3/C_3N_4 composites, both the bands of C_3N_4 and In_2O_3 can be observed and the characteristic absorption peak of In_2O_3 became more and more obvious with the increasing content of In_2O_3. Therefore, on the basis of XRD, XPS and FT-IR analysis, the presence of In_2O_3 and C_3N_4 species was confirmed in composites.

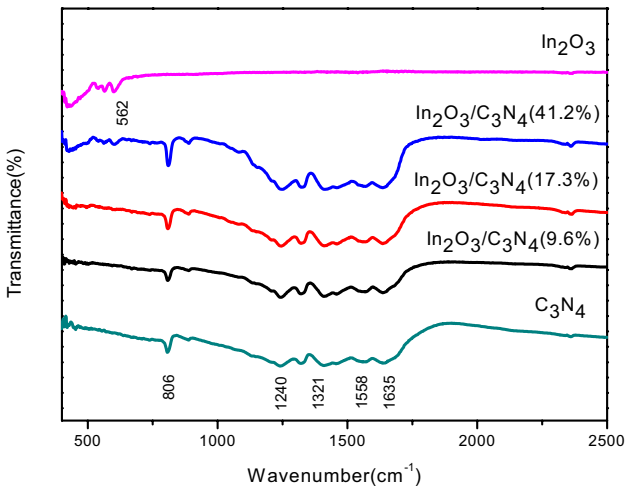

Fig. 5 FT-IR spectra of In_2O_3, C_3N_4, and In_2O_3/C_3N_4 composites

3.6 DRS analysis

Figure 6 showed the UV–Vis DRS of In_2O_3, C_3N_4 and In_2O_3/C_3N_4 composites. The absorption band edge was about 440 nm and 460 nm for In_2O_3 and C_3N_4 [38, 39], respectively. Compared with In_2O_3, the absorption bands edge of In_2O_3/C_3N_4 composites red-shifted and showed clear visible light response. The red-shifting of absorption band edge meant that the photocatalysis can produce more electron and holes under the stimulation of the visible light, which was beneficial to enhance the catalytic activity. The forbidden band width of semiconductor photocatalytic materials can be presented as followed formula:

$$\alpha h\nu = A(h\nu - Eg)^n$$

where α is absorption coefficient, h is Planck constant, ν is frequency of light, A is semiconductor material constants, Eg is forbidden band width and n is constant (usually direct bandwidth material n = 1/2, indirect bandwidth material n = 2 [40]). In_2O_3 belongs to direct bandwidth material and C_3N_4 belongs to indirect bandwidth material, so the value of n take 1/2 and 2, respectively. The E_g of C_3N_4 and In_2O_3 can be estimated form the forbidden band width spectra of In_2O_3 and C_3N_4 (Fig. 6b), which was drew by using $(\alpha h\nu)^{1/n}$ as ordinate and hν as abscissa. The intersection point of the tangent to the curve and abscissa is the Eg of material. The estimated forbidden band width of In_2O_3 and C_3N_4 were 2.78 eV and 2.70 eV. The result was in agreement with the literature [41, 42].

3.7 Photocatalytic activity

The organic pollutant MO was chosen to evaluate the photocatalytic performance of In_2O_3/C_3N_4 composites, and the

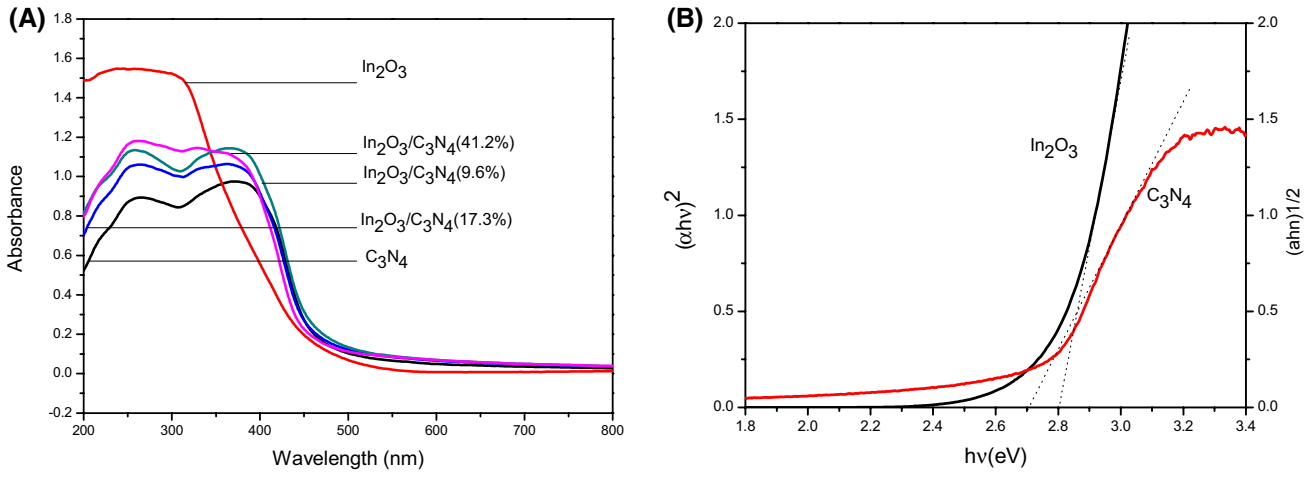

Fig. 6 **A** UV–Vis DRS of C_3N_4, In_2O_3 and In_2O_3/C_3N_4 composites; **B** The plot of $(\alpha h\nu)^2$ versus energy (hν) for the band gap energy of In_2O_3 and the plot of $(\alpha h\nu)^{1/2}$ versus energy (hν) for the band gap energy of C_3N_4

result was shown in Fig. 7. The photocatalytic performance of In_2O_3 and C_3N_4 were comparatively low, only 12.1% and 20.8% MO were degraded when the irradiation time lasted for 3 h (Fig. 7A), respectively. However, most of the In_2O_3/C_3N_4 composites displayed much higher photocatalytic activity than C_3N_4 and In_2O_3. Upon increasing the content of In_2O_3, the photocatalytic activity first increased and then decreased. In_2O_3/C_3 N_4 (17.3%) composite showed the optimal photocatalytic performance among all composites. The reason may be that when the In_2O_3 content was too high, In_2O_3 nanoparticles had self-agglomeration and reduce the contact interface and heterojunction structure between In_2O_3 and C_3N_4. It leads to the decrease of electrons and holes separation efficiency, which weakens the photocatalytic activity. The removal rate of MO was about 61% for In_2O_3/C_3 N_4 (17.3%) after 3 h. The temporal evolution of the absorption spectra of MO catalyzed by In_2O_3, C_3N_4 and In_2O_3/C_3 N_4 (17.3%) composites is illustrated in Fig. 7B, C, D. For C_3N_4 or In_2O_3, the MO degradation was quite slow and the MO could not be distinctly degraded after 3 h (Fig. 7B, C). However, the absorption peak at 464 nm decreased obviously within 3 h (Fig. 7D) for In_2O_3/C_3 N_4 (17.3%) composite, which indicated that In_2O_3/C_3 N_4 (17.3%) sample exhibited high photocatalytic activity. Therefore, the photocatalytic activity of both C_3N_4 and In_2O_3 were lower than In_2O_3/C_3 N_4 (17.3%) sample under the experimental conditions.

3.8 Photocurrent and EIS analysis

The photoproduction electron holes efficiency of In_2O_3, C_3N_4 and In_2O_3/C_3 N_4 (17.3%) composite can be performed through the transient photocurrent response experiment. As shown in Fig. 8A, the samples can rapidly generate photocurrent when the light is on, suggesting that there were charge carriers in samples. The photocurrent of In_2O_3/C_3N_4 (17.3%) composite was higher than that of In_2O_3 and C_3N_4. The photocurrent response to In_2O_3/C_3 N_4 (17.3%) composite was 11.3 times and 183.1 times as that of pure In_2O_3 and C_3N_4, respectively. The result showed that In_2O_3/C_3 N_4

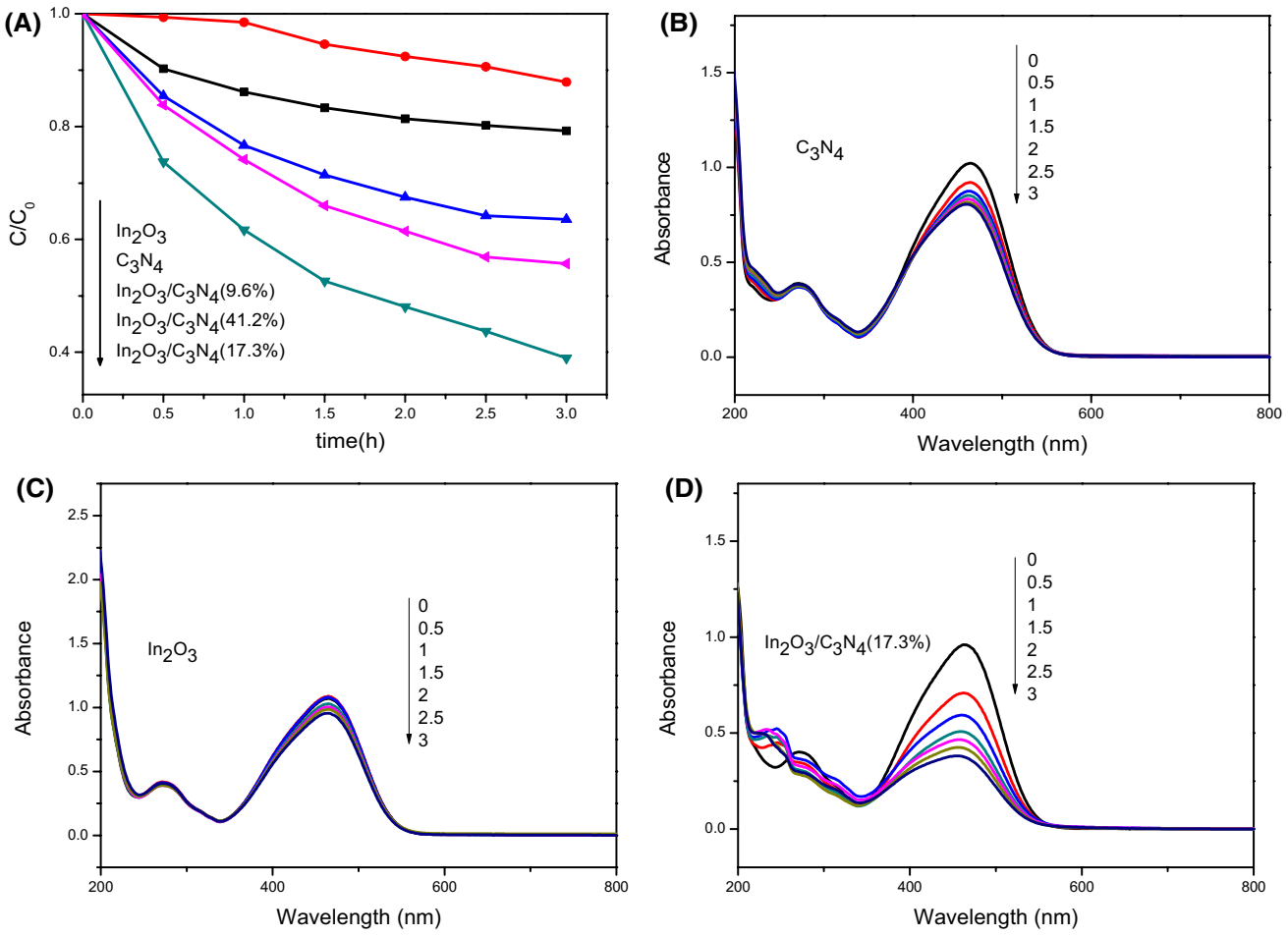

Fig. 7 **A** Photodegradation of MO on In_2O_3/C_3N_4 composites, **B** C_3N_4, **C** In_2O_3 and **D** changes in absorption spectra of MO by C_3N_4, In_2O_3 and In_2O_3/C_3 N_4 (17.3%) composite

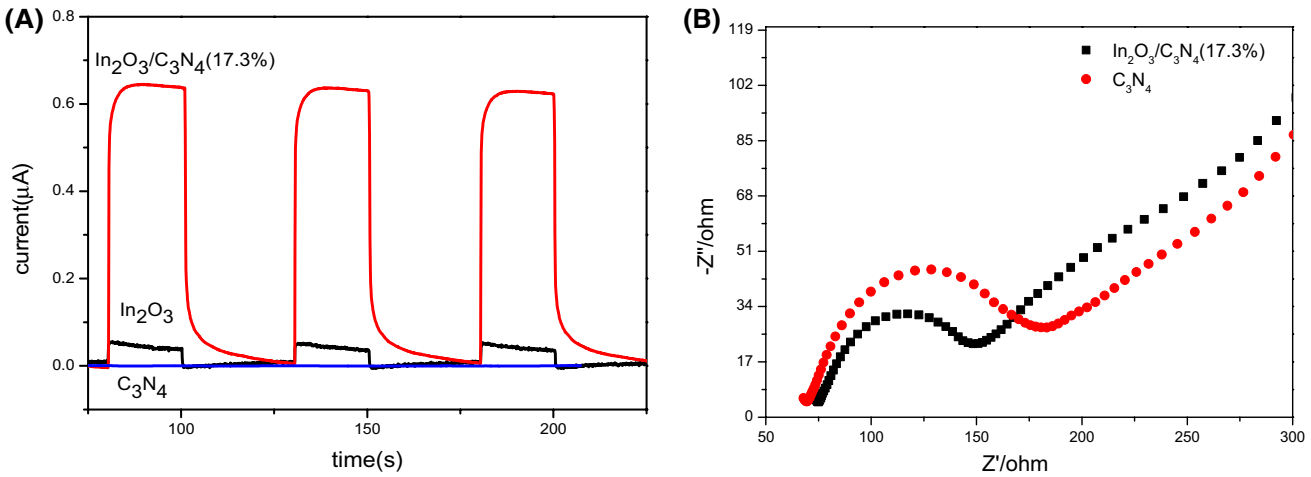

Fig. 8 **A** Transient photocurrent response for pure C_3N_4, In_2O_3 and In_2O_3/C_3 N_4 (17.3%) composite; **B** EIS profiles of C_3N_4 and In_2O_3/C_3 N_4 (17.3%) composite

(17.3%) composite had low electron–hole recombination rate and also confirmed that the introduction to In_2O_3 in C_3N_4 can effectively improve the electron–hole separation efficiency to enhance the photocatalytic activity. According to this result, the formation of heterojunction was beneficial to the charge separation and enhancement of photocatalytic activity [43].

EIS measurement was also employed to investigate the charge transfer and the separation efficiency between the photogenerated electrons and holes. From Fig. 8B, it could be observed that the diameter of the Nquist circle of In_2O_3/C_3 N_4 (17.3%) composite was smaller than that of C_3N_4. It indicated that In_2O_3/C_3N_4 (17.3%) composite had lower resistance than that of C_3N_4. This result confirmed that the introduction In_2O_3 into C_3N_4 can enhance the separation and transfer efficiency of photogenerated electron–hole pairs [44], which was benefit to the enhancement of photocatalytic activity.

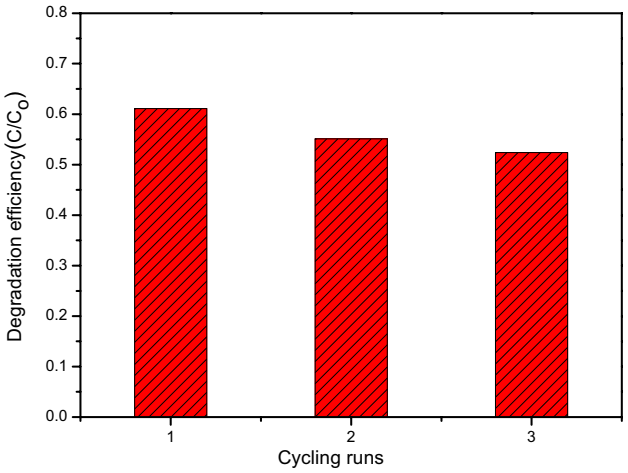

Fig. 9 Cycling runs of In_2O_3/C_3 N_4 (17.3%) composite under visible light irradiation for 3 h

3.9 Stability evaluation

Except photocatalytic efficiency, another important evaluation criterion of catalyst is the stability. The cyclic photocatalytic degradation of MO was carried out to investigate the recyclability of In_2O_3/C_3N_4 and the result was shown in Fig. 9. The photocatalytic activity of In_2O_3/C_3 N_4 (17.3%) showed a slight loss after 3 recycles, which was ascribed to the loss of photocatalyst.

3.10 Photoluminescence spectra analysis

Photoluminescence (PL) emission spectra of C_3N_4 and In_2O_3/C_3 N_4 (17.3%) composite was shown in Fig. 10 to study the efficiency of charge transfer and electron–hole pairs separation. For the pure C_3N_4, an emission peak at about 460 nm was attributed to the band gap energy of C_3N_4 (2.7 eV) [45]. In addition, the peak of In_2O_3/C_3 N_4 (17.3%) composite was weaker than that of pure C_3N_4, suggesting the efficient inhibition of the recombination between charge carriers. The decrease of electron–hole recombination enhanced the photocatalytic activity for degradation of pollution.

3.11 Detection of reactive species

In order to investigate the mechanism, reactive species trapping experiments were carried out to investigate the

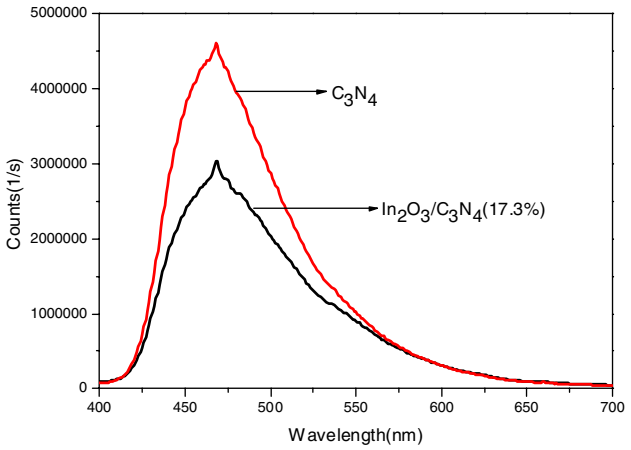

Fig. 10 Photoluminescence (PL) spectra of C_3N_4 and In_2O_3/C_3N_4 (17.3%) composite

main active oxygen species during the degradation process. In_2O_3/C_3N_4 (17.3%) was selected for testing. As shown in Fig. 11, when N_2 was used to scavenger $\cdot O_2^-$, the photocatalytic activity decreased a lot. This phenomenon indicated that $\cdot O_2^-$ played an important role in the degradation process. The scavenger triethanolamine (TEOA) was chosen for catching holes (h^+) and the photocatalytic activity was significantly decreased, which meant that h^+ also played a role in the degradation. However, the photocatalytic performance did not change with the addition of isopropanol (IPA) as the scavenger for ·OH. The result suggested that ·OH was not the major oxidative species in the photocatalytic reaction. In conclusion, the reactive species were $\cdot O_2^-$ and h^+ during the photo-degradation process.

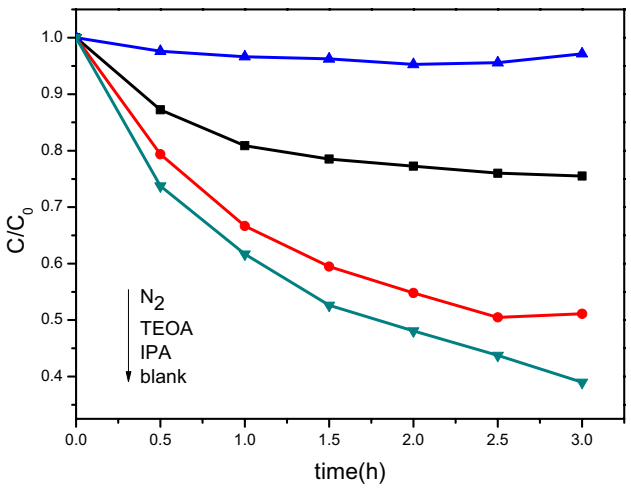

Fig. 11 Reactive species trapping experiments over In_2O_3/C_3N_4 (17.3%) composite

3.12 Possible photocatalytic mechanism

The high efficiency of charge separation was an important factor for the significant enhancement of photocatalytic activity. However, effectively separation of electron and holes depended on whether the two kinds of semiconductor materials had suitable position of band gaps. It was conducive to the separation of electrons and holes due to the suitable band gap structure of two kinds of semiconductor materials [44]. According to the structure characteristics and the photocatalytic performance tests of C_3N_4/In_2O_3 composite, a possible mechanism was presented and showed in Fig. 12. For semiconductors, the conduction bands and valence bands can be expressed as following equation:

$$E_{CB}^0 = \chi + E^C - 1/2E_g$$

where χ is absolute electronegativity of the semiconductor (χ is 5.28 eV for In_2O_3 [46]), E^C is energy of free electrons on the hydrogen scale (−4.5 eV [47]), E_g is band gap of the semiconductor. According to Fig. 6B, the band gaps of C_3N_4 and In_2O_3 were 2.70 eV and 2.68 eV, respectively. The calculated top VB and bottom CB of In_2O_3 were 2.12 eV and −0.56 eV, respectively. For C_3N_4, the top VB and the bottom CB were 1.57 eV and −1.13 eV, respectively [44]. Upon irradiated by visible light (>400 nm), both In_2O_3 and C_3N_4 can be activated in the composites. Since CB of C_3N_4 (−1.13 eV) was lower than that of In_2O_3 (−0.56 eV), the excited electrons at the CB of C_3N_4 crystallites could transfer to the CB of In_2O_3 crystallites and the photogenerated holes on In_2O_3 could move to C_3N_4 via the hybrid interface. Thus, this suppressed the charge recombination easily, which resulted in the enhancement of photocatalytic performance.

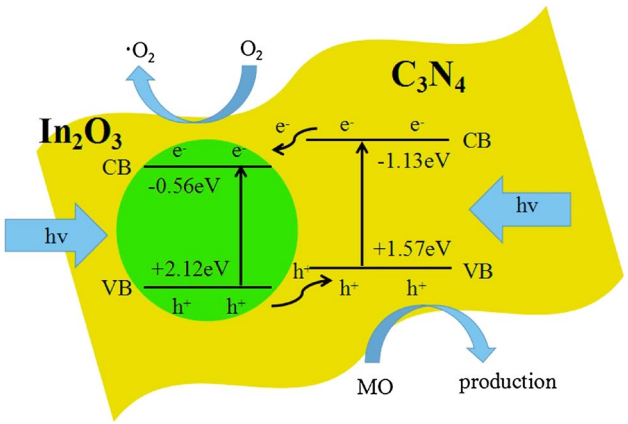

Fig. 12 Proposed mechanism for the photodegradation of pollutants on In_2O_3/C_3N_4 composites

4 Conclusions

In summary, via a ballmilling-calcination method, In_2O_3/C_3N_4 composite photocatalysis has been prepared. The optimum sample In_2O_3/C_3 N_4 (17.3%) composite can degrade 61% MO within 3h under visible light, while pure In_2O_3 and C_3N_4 only degrade 12.1% and 20.8% MO, respectively. The synergy effects between In_2O_3 and C_3N_4 may be the reason for enhanced photocatalytic activity. The experiment results showed $\cdot O_2^-$ and h^+ were the reactive species during the degradation process. The efficient synthesis method of In_2O_3/C_3N_4 composites has significant interest in pollutants degradation and it offers a convenient method to synthesis new photocatalysts with high performance in environmental protection.

Acknowledgements The authors genuinely appreciate the financial support of this work from the National Nature Science Foundation of China (21406094), Postdoctoral Foundation of China (2015M571693) and Foundation of Jiangsu University (14JDG184).

References

1. N. Beji, M. Souli, S. Azzaza, S. Alleg, N.K. Turki, J. Mater. Sci. **27**, 4849–4860 (2016).
2. Y. Zhang, J.Q. Zhang, M.Y. Nie, K. Sun, J.Q. Li, C.H. Yu, J. Nanopart. Res. **17**, 1–11 (2015)
3. M.C. Qin, J.J. Ma, W.J. Ke, P.L. Qin, H.W. Lei, H. Tao, X.L. Zheng, L.B. Xiong, Q. Liu, Z.L. Chen, J.Z. Lu, G. Yang, G.J. Fang, ACS Appl. Mater. Interfaces **8**, 8460–8466 (2016)
4. E. Medvedovski, N.A. Alvarez, C.J. Szepesi, O. Yankov, P. Lippens, Adv. Appl. Ceram. **112**, 243–256, (2013).
5. A. Ilin, M. Martyshov, E. Forsh, P. Forsh, M. Rumyantseva, A. Abakumov, A. Gaskov, P. Kashkarov, Sens. Actuators B. **23**, 491–496, (2016).
6. J.M. Yang, Z.P. Qi, Y.S. Kang, Q. Liu, W.Y. Sun, Chin. Chem. Lett. **27**, 492–496 (2016)
7. F. Zhao, Q.F. Lu, Z.L. Xiu, C.F. Zhu, Nano **11**, 110–119 (2016).
8. M. Karmaoui, S.G. Leonardi, M. Latino, D.M. Tobaldi, N. Donato, R.C. Pullar, M.P. Seabra, J.A. Labrincha, G. Neri, Sens. Actuators B. **230**, 697–705 (2016)
9. Z.F. Jiang, D.L. Jiang, Z.X. Yan, D. Liu, K. Qian, J.M. Xie, Appl. Catal. B. **170–171**, 195–205 (2015)
10. H.R. Liu, X. He, Y.C. Hu, X.G. Liu, H.S. Jia, B.S. Xu, Mater. Lett. **131**, 104–107 (2014)
11. L.Y. Chen, W.D. Zhang, Appl. Surf. Sci. **301**, 428–435 (2014)
12. Z.Y. Liang, Q.J. Wen, X. Wang, F.W. Zhang, Y. Yu, Appl. Surf. Sci. **386**, 451–459 (2016)
13. S.M. Lam, J.C. Sin, A.R. Mohamed, Mater. Sci. Semicond. Process. **47**, 62–84 (2016).
14. S.L. Ma, S.H. Zhan, Y.N. Jia, Q. Shi, Q.X. Zhou, Appl. Catal. B. **186**, 77–87 (2016)
15. M.J. Muñoz-Batista, O. Fontelles-Carceller, M. Ferrer, M. Fernández-García, A. Kubacka, Appl. Catal. B. **183**, 86–95 (2016)
16. S. Tonda, S. Kumar, V. Shanker, Mater. Res. Bull. **75**, 51–58 (2016)
17. S.F. Kang, Y. Fang, Y.K. Huang, L.F. Cui, Y.Z. Wang, H.F. Qin, Y.M. Zhang, X. Li, Y.G. Wang, Appl. Catal. B. **168–169**, 472–482 (2015)
18. T. Zhou, Y.G. Xu, H. Xu, H.F. Wang, Z.L. Da, S.Q. Huang, H.Y. Ji, H.M. Li, Ceram. Int. **40**, 9293–9301 (2014).
19. Y.F. Li, Y. Zhao, L. Fang, R.X. Jin, Y. Yang, Y. Xing, Mater. Lett. **126**, 5–8 (2014)
20. R.C. Pawar, Y. Son, J. Kim, S.H. Ahn, C.S. Lee, Curr. Appl Phys. **16**, 101–108 (2016).
21. S.W. Cao, Y.P. Yuan, J. Fang, M.M. Shahjamali, F.Y.C. Boey, J. Barber, S.C. Joachim Loo, C. Xue, Int. J. Hydrog. Energy **38**, 1258–1266 (2013)
22. J.Q. Li, H.J. Hao, Z.F. Zhu, Mater. Lett. **168**, 180–183 (2016)
23. C.C. Han, L. Ge, C.F. Chen, Y.J. Li, X.L. Xiao, Y.N. Zhang, L.L. Guo, Appl. Catal. B. **147**, 546–553 (2014)
24. L. Liu, Y.H. Qi, J.R. Lu, S.L. Lin, W.J. An, Y.H. Liang, W.Q. Cui, Appl. Catal. B. **183**, 133–141 (2016)
25. Z.C. Yang, J. Li, F.X. Cheng, Z. Chen, X.P. Dong, J. Alloys Compd. **634**, 215–222 (2015)
26. S. Yin, J. Di, M. Li, Y.L. Sun, J.X. Xia, H. Xu, W.M. Fan, H.M. Li, J. Mater. Sci. **51**, 4769–4777 (2016)
27. J.C. Wang, H.C. Yao, Z.Y. Fan, L. Zhang, J.S. Wang, S.Q. Zang, Z.J. Li, ACS Appl. Mater. Interfaces **8**, 3765–3775 (2016)
28. J.B. Sun, J.R. Song, M.A. Gondal, S. Shi, Z.X. Lu, Q.Y. Xu, X.F. Chang, D.H. Xiang, K. Shen, Res. Chem. Intermed. **41**, 6941–6955 (2014)
29. Y.P. Zang, L.P. Li, X.G. Li, R. Lin, G.S. Li, Chem. Eng. J **246**, 277–286 (2014)
30. S.W. Cao, X.F. Liu, Y.P. Yuan, Z.Y. Zhang, Y.S. Liao, J. Fang, S.C.J. Loo, T.C. Sum, C. Xue, Appl. Catal. B. **147**, 940–946 (2014)
31. A. Aoki, H. Ohtake, T. Shimizu, Energy **25**, 201–208 (2000)
32. S.C. Yan, Z.S. Li, Z.G. Zou, Langmuir **25**, 10397–10401 (2009)
33. S. Zhang, P. Song, H.H. Yan, Q. Wang, Sens. Actuators B. **231**, 245–255 (2016)
34. Q. Liu, W. Zhang, R.M. Liu, G.B. Mao, Eur. J. Inorg. Chem. **2015**, 845–851 (2015)
35. M. Wang, Z.L. Liu, M.H. Fang, C. Tang, Z.H. Huang, Y.G. Liu, X.W. Wu, Y.J. Mao, Solid State Sci. **55**, 1–7 (2016).
36. F.M. Qiao, Q.Q. Qi, Z.Z. Wang, K. Xu, S.Y. Ai, Sens. Actuators B. **229**, 379–386 (2016)
37. K.R. Devi, S.D. Meetei, S.D. Singh, Mater. Charact. **114**, 197–203 (2016).
38. Y.D. Guo, Z.H. Gong, P. Li, W.M. Zhang, B. Gao, Ceram. Int. **42**, 8850–8855 (2016).
39. J.Y. Liu, J. Yan, H.Y. Ji, Y.G. Xu, L.Y. Huang, Y.P. Li, Y.H. Song, Q. Zhang, H. Xu, H.M. Li, Mater. Sci. Semicond. Process. **46**, 59–68 (2016).
40. F. Zhang, X.Y. Li, Q.D. Zhao, Q.Z. Zhang, M. Tade, S.M. Liu, J. Colloid Interface Sci. **457**, 18–26 (2015)
41. J. Feng, T.T. Chen, S.N. Liu, Q.H. Zhou, Y.M. Ren, Y.Z. Lv, Z.J. Fan, J. Colloid Interface Sci. **479**, 1–6 (2016)
42. L.L. Xu, L. Ni, W.D. Shi, J.G. Guan, Chin. J. Catal. **33**, 1101–1108 (2012)
43. T.T. Li, L.H. Zhao, Y.M. He, J. Cai, M.F. Luo, J.J. Lin, Appl. Catal. B. **129**, 255–263 (2013)
44. L.Y. Huang, H. Xu, Y.P. Li, H.M. Li, X.N. Cheng, J.X. Xia, Y.G. Xu, G.B. Cai, Dalton Trans. **42**, 8606–8616 (2013)
45. Y.P. Li, L.Y. Huang, J.B. Xu, H. Xu, Y.G. Xu, J.X. Xia, H.M. Li, Mater. Res. Bull. **70**, 500–505 (2015)

46. H.H. Li, C. Chen, X.Y. Huang, Y. Leng, M.N. Hou, X.G. Xiao, J. Bao, J.L. You, W.W. Zhang, Y.K. Wang, J. Song, Y.P. Wang, Q.Q. Liu, G.A. Hope, J. Power Sources **247**, 915–919 (2014)
47. X. Chen, L. Li, W.Z. Zhang, Y.X. Li, Q. Song, J.Q. Zhang, D. Liu, J. Mol. Catal. A. **414**, 27–36 (2016)